# Supplemental Material for "Extensive Spatio-Temporal Chaos in Non-reciprocal Flocking"

## CONTENTS



## I. PHASE DIAGRAM AND CLASSIFICATION

This section provides supplementary details for the microscopic phase behavior summarized in Fig. 1(m) of the main text. We first present additional representative late-time snapshots across the $(J_+, J_-)$ plane and fix the terminology used for the observed states. We then describe the operational criteria used to assign each parameter point in the phase diagram. Finally, we explain how the mean-field exceptional line shown in Fig. 1(m) is obtained in the normalization convention of our microscopic model.

### A. Phases and representative snapshots

Figure 1 collects additional late-time microscopic snapshots across the $(J_+, J_-)$ plane. In the data shown here, we restrict attention to the half-plane $J_- > 0$, where species $A$ tends to align with $B$, while species $B$ tends to anti-align with $A$. The observed behaviors can be organized into five representative late-time states: two homogeneous ordered states, two inhomogeneous ordered states, and a chaotic state.

The homogeneous ordered states are the parallel-flocking (PF) and antiparallel-flocking (AF) phases. In both cases, the two species remain spatially well mixed, and the density field stays nearly uniform apart from weak fluctuations. The distinction between them lies primarily in the relative orientation of the global polarizations: in the PF state the two species move in the same direction, whereas in the AF state they move in opposite directions. For fixed positive $J_-$, these homogeneous states are found at sufficiently large $|J_+|$, with PF and AF located on opposite sides of the phase diagram.

The inhomogeneous ordered states are the species-separated PF band and longitudinal AP lane sectors. In the PF band sector, the two species remain globally parallel but segregate into a banded configuration in which $A$ species forms a much more compact band than $B$ species, producing a density modulation transverse to the mean

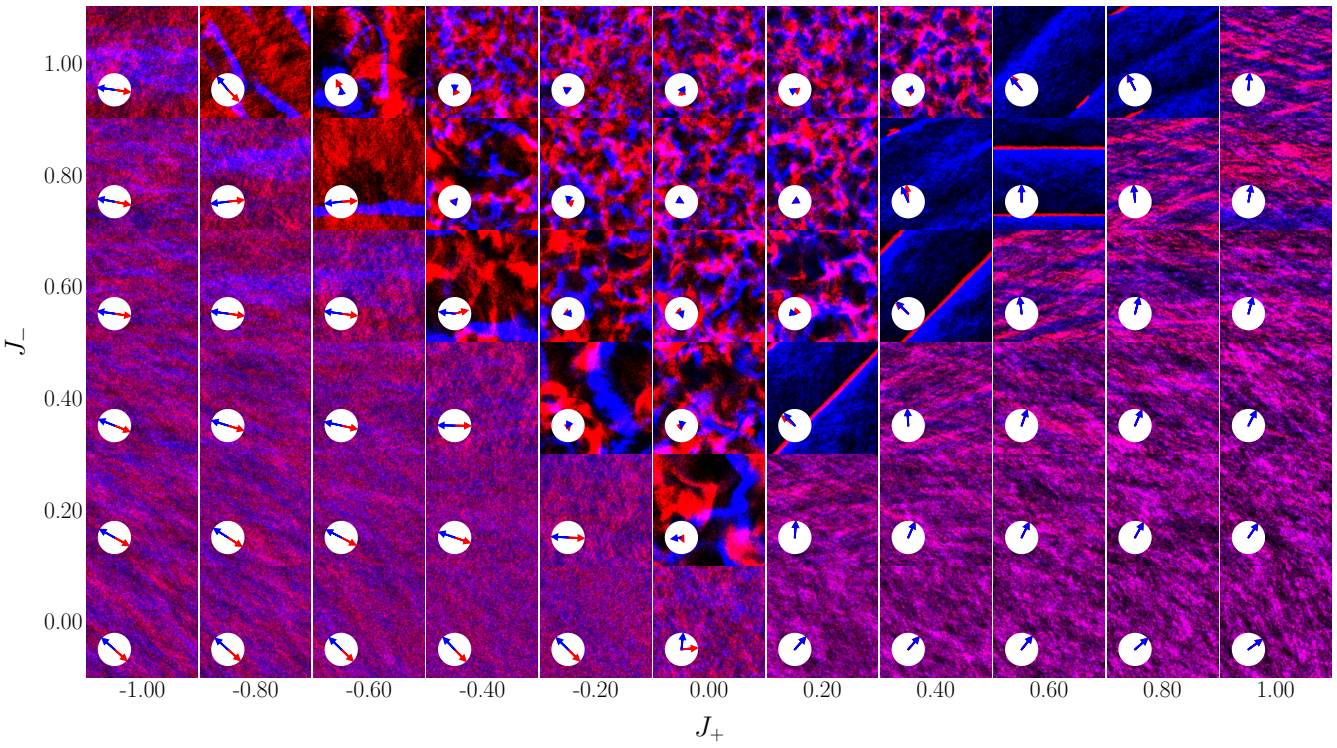


FIG. 1. Representative late-time snapshots across the $(J_+, J_-)$ plane at $T = 0.1$, $\rho_A = \rho_B = 3$ and $L = 256$. Each panel shows the coarse-grained density field together with the instantaneous global polarizations of the two species.

propagation direction. In the AF lane sector, the two species move antiparallel and organize into a longitudinal lane structure in which $B$ species forms a dense lane against a more diffuse background of the $A$ species, yielding density modulations parallel to the mean propagation direction. Along a cut at fixed $J_- > 0$, these structured sectors appear at intermediate values of $J_+$, between the homogeneous PF/AF states at large $|J_+|$ and the more irregular regime near $J_+ = 0$.

Between these ordered sectors lies a chaotic regime characterized by strong spatial heterogeneity, local species segregation, and persistent temporal fluctuations. These states do not relax into either homogeneous PF/AF order or a stable banded/lane structure, but instead remain dynamically disordered at late times. This regime is concentrated where $|J_+| \lesssim J_-$, most prominently near the antisymmetric line $J_+ = 0$ for $J_- > 0$.

A comparison with the weakly non-reciprocal mixtures studied by Myin and Mahault [1] suggests that all of the main late-time states observed here have qualitative counterparts in their phase diagram: homogeneous PF and AF states, a demixed PF state corresponding to their single-band regime, an AF laning regime, and a chaotic regime. The coexistence-band states reported there but not resolved in our present parameter range appear near the onset of order. This likely reflects the different parameter scans used in the two works. Our phase diagram is constructed at fixed low noise while scanning the $(J_+, J_-)$ plane in a parameter range with already robust intra-species ordering, so that we predominantly probe states well inside the ordered regime. By contrast, Ref. [1] organizes its phase diagram in the nonreciprocity-noise plane and therefore resolves coexistence-band states specifically in the near-threshold region where order first emerges.

### B. Phase classification

To classify each point in the phase diagram, we use two late-time observables: one characterizing the relative orientation of the global polarizations of the two species, and the other characterizing the degree of species segregation in the coarse-grained density field.

The relative alignment of the two species is quantified by

$$C = \boldsymbol{V}_A \cdot \boldsymbol{V}_B, \tag{1}$$

where $\boldsymbol{V}_A$ and $\boldsymbol{V}_B$ are the species-resolved averages of the microscopic heading vectors $\boldsymbol{u}_i = (\cos\theta_i, \sin\theta_i)$ for particles of species $A$ and $B$, respectively. After discarding the transient part of the trajectory, we characterize the asymptotic state by the late-time average $\overline{C}$. Positive $\overline{C}$ indicates parallel collective motion, whereas negative $\overline{C}$ indicates antiparallel collective motion.

To quantify species segregation, we examine the coarse-grained density field. Writing the coarse-grained

particle densities of the two species as $\rho_A(\boldsymbol{r})$ and $\rho_B(\boldsymbol{r})$, with $\boldsymbol{r}$ running over coarse-graining boxes of size $1 \times 1$, we define

$$N_{\pm} = \left|\left\{\boldsymbol{r} : \pm\big(\rho_A(\boldsymbol{r}) - \rho_B(\boldsymbol{r})\big) > 0\right\}\right|. \tag{2}$$

Thus, $N_+$ and $N_-$ count the boxes locally dominated by species $A$ and $B$, respectively. For phase classification we use the corresponding late-time averages, denoted by $\overline{N_{\pm}}$. A pronounced imbalance between $\overline{N_+}$ and $\overline{N_-}$ serves as a practical indicator of species segregation, whereas comparable values indicate that the two species remain more uniformly mixed.

The phase assignment used for Fig. 1(m) in the main text is implemented in two steps. We first use $\overline{C}$ to determine whether the late-time state exhibits global PF or AF order. States with $\overline{C} > C_{\mathrm{th}}$ are assigned to the PF sector, whereas states with $\overline{C} < -C_{\mathrm{th}}$ are assigned to the AF sector. If $|\overline{C}| \le C_{\mathrm{th}}$, the state is not regarded as globally ordered and is assigned to the chaotic regime.

We then use the segregation measure to distinguish homogeneous and structured states within the ordered PF and AF sectors. This second step is motivated by the late-time snapshots: in the structured sectors, one species typically forms a relatively compact band or lane, while the other remains distributed more diffusely in the surrounding background. The relative magnitude of $\overline{N_+}$ and $\overline{N_-}$ provides a simple proxy for this asymmetry in spatial localization.

Within the PF sector, a state is classified as a species-separated band state if $\overline{N_-} > R_{\mathrm{th}}\overline{N_+}$, and as homogeneous PF otherwise. This criterion selects PF states in which $B$ species is much more strongly concentrated into a transverse band than $A$ species. Within the AF sector, a state is classified as a AP lane state if $\overline{N_+} > R_{\mathrm{th}}\overline{N_-}$, and as homogeneous AF otherwise. This criterion likewise selects AF states in which $A$ species forms a pronounced longitudinal lane against a more diffuse background of $B$ species.

In practice, we use $C_{\mathrm{th}} = 0.5, R_{\mathrm{th}} = 3$. This classification thresholds are heuristic and chosen to reproduce the visually identified late-time states.

### C. Comparison with the mean-field exceptional line

The thick line in Fig. 1(m) shows the exceptional transition line obtained from the spatially homogeneous mean-field dynamics. Because the derivation closely follows that of Ref. [2], we summarize here only the modification specific to our microscopic model.

In our model, each alignment interaction is normalized by the local number of neighbors $N_i^{\alpha}$. Under the homogeneous mean-field assumption, spatial gradients are neglected and the coarse-grained polarization fields are taken to be uniform, so that

$$N_i^{\alpha} \simeq \rho_{\alpha}\pi R^2. \tag{3}$$

This neighbor factor then cancels between numerator and denominator, so that the homogeneous dynamics is governed directly by the bare couplings $J_{ab}$, rather than by the combinations $j_{ab}\rho_b$ appearing in Ref. [2]. Equivalently, the mean-field equations retain the same algebraic structure as in the reference theory under the replacement

$$j_{ab}\rho_b \to J_{ab}. \tag{4}$$

With this replacement, the homogeneous dynamics can be written in terms of the nonlinear matrix

$$\hat{W}_0 = \begin{pmatrix} W^0_{AA} & J_{AB} \\ J_{BA} & W^0_{BB} \end{pmatrix}, \tag{5}$$

where

$$\begin{aligned} W^0_{AA} &= -T + J_{AA} - \frac{1}{2T}\left\|J_{AA}\mathbf{P}_A + J_{AB}\mathbf{P}_B\right\|^2, \\ W^0_{BB} &= -T + J_{BB} - \frac{1}{2T}\left\|J_{BA}\mathbf{P}_A + J_{BB}\mathbf{P}_B\right\|^2. \end{aligned} \tag{6}$$

For the case of symmetric self-couplings, we define

$$\bar{W}_0 = W^0_{AA} + W^0_{BB}, \qquad \Delta W_0 = W^0_{AA} - W^0_{BB}. \tag{7}$$

The two eigenvalues of $\hat{W}_0$ are then

$$\Gamma_{\pm} = \frac{\bar{W}_0 \pm \sqrt{\lambda_0}}{2}, \qquad \lambda_0 = (\Delta W_0)^2 + 4J_{AB}J_{BA}. \tag{8}$$

As in Ref. [2], the sign of $\lambda_0$ determines the nature of the homogeneous ordered state. When $\lambda_0 > 0$, the eigenvalues are real and the ordered solution is static, whereas $\lambda_0 < 0$ yields a complex-conjugate pair and hence an oscillatory chiral state. The boundary between these two regimes is the exceptional point, defined by

$$\Gamma_- = 0, \qquad \lambda_0 = 0. \tag{9}$$

Together, these conditions determine the exceptional transition line plotted in Fig. 1(m), which we include as the homogeneous mean-field reference for the onset of oscillatory order.

## II. DECAY TIME AND DROPLET-TRIGGERED COLLAPSE

This section provides supplementary details for the decay of the prepared homogeneous chiral state summarized in Fig. 2(b) of the main text. We first define the operational criterion used to extract the decay time and present additional survival-probability data. We then introduce the droplet-seeding protocol used to probe the local fragility of the homogeneous chiral state and to estimate the corresponding critical radius.

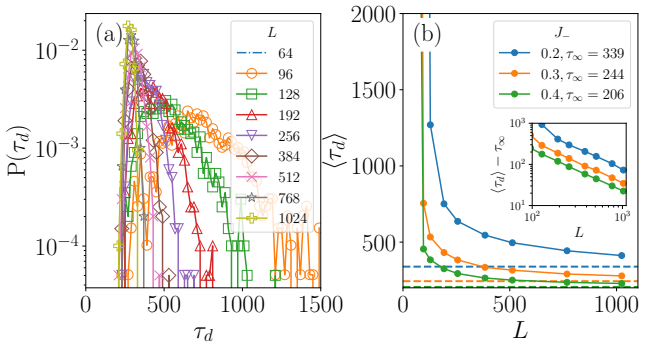


FIG. 2. (a) Distributions $P(\tau_d)$ for increasing system size at fixed $J_- = 0.2$. (b) Mean decay time $\langle \tau_d \rangle$ versus $L$ for $J_- = 0.2, 0.3$, and 0.4. The dashed horizontal lines indicate the thermodynamic-limit timescales $\tau_\infty$ obtained from fits to $\langle \tau_d(L) \rangle = \tau_\infty + a/L$. The inset shows $\langle \tau_d(L) \rangle - \tau_\infty$.

### A. Definition of the decay time

To quantify the decay of the homogeneous chiral state, we measure an onset time $\tau_d$ from trajectories initialized in the prepared homogeneous rotating state. As in the main text, $\tau_d$ is defined as the first time at which the initially homogeneous rotating state undergoes a local irreversible breakdown, signaling the onset of the macroscopic collapse.

Operationally, we coarse-grain the system into square boxes of linear size $4 \times 4$ and monitor the local species densities $\rho_\alpha(\boldsymbol{r}, t)$ defined as the particle numbers in each box divided by the box area. Let $\rho_0$ denote the mean density of each species in the homogeneous background. We identify a local breakdown event whenever at least one coarse-graining box satisfies

$$\rho_A(\boldsymbol{r}, t) > R_{\rm nuc}\rho_0, \quad \rho_B(\boldsymbol{r}, t) < \rho_0/R_{\rm nuc}, \tag{10}$$

where $R_{\rm nuc}$ denotes the density threshold. To exclude short-lived fluctuations, the threshold condition must persist continuously for a persistence window $\tau_{\rm pers} = 10$. The decay time $\tau_d$ is then defined as the first time at which this criterion is met and remains satisfied for a duration $\tau_{\rm pers}$. We use $R_{\rm nuc} = 3$; stricter choices do not qualitatively change the result.

### B. Size dependence of a mean decay time

The probability distributions $P(\tau_d)$ of the decay time are shown in Fig. 2 (a) for several values of $L$ at fixed $J_- = 0.2$. As the system size increases, the distributions narrow and shift toward a small $\tau_d$ side. Figure 2(b) shows that the mean decay time is well described by a finite-size scaling form

$$\langle \tau_d(L) \rangle = \tau_\infty + \frac{a}{L} \tag{11}$$

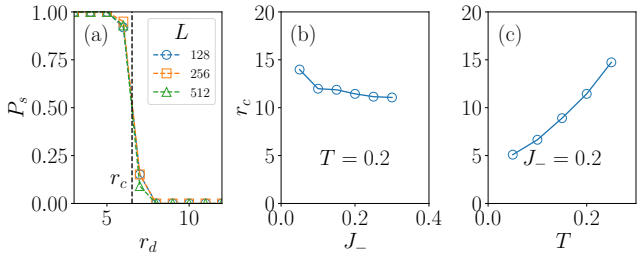


FIG. 3. Critical droplet radius for the breakdown of the homogeneous chiral state. (a) Survival probability $P_s$ as a function of the droplet radius $r_d$ for several system sizes; the dashed line marks the characteristic radius $r_c$. (b) Characteristic radius $r_c$ as a function of $J_-$ at fixed $T = 0.2$. (c) Characteristic radius $r_c$ as a function of the noise strength $T$ at fixed $J_- = 0.2$.

with a finite decay time in the thermodynamic limit. This result allows us to interpret that the homogeneous chiral state is destabilized by an finite length instability with a finite thermodynamic-limit timescale.

### C. Droplet-seeding protocol and critical radius

To probe the local fragility of the homogeneous chiral state, we seed a circular droplet of radius $r_d$ inside a prepared homogeneous rotating background. The background state is initialized with a relative phase shift $\Delta\phi = \frac{\pi}{2}$ between the two species. Inside the seeded droplet, the densities of both species are increased by a factor of five relative to the homogeneous background, and the local polarization of both species is rotated by $\pi$.

After this local perturbation is imposed, the dynamics is resumed and monitored for a fixed observation time $\tau_m = 100$, chosen to be shorter than the spontaneous breakdown timescale $\tau_\infty$. A seeded run is classified as surviving if no onset event, according to the criterion defined above, is detected during the interval $[0, \tau_m]$. Otherwise it is classified as failed. The corresponding survival probability $P_s(r_d)$ is the fraction of seeded runs that survive up to time $\tau_m$.

As shown in Fig. 3(a), $P_s(r_d)$ exhibits a sharp crossover as a function of the droplet radius, which allows us to define a characteristic radius $r_c$. Droplets with $r_d < r_c$ typically shrink and disappear, whereas droplets with $r_d > r_c$ trigger the same spatially heterogeneous chiral state seen in spontaneous breakdown events. The characteristic radius remains finite as the system size is increased from $L = 128$ to 512.

Panels (b) and (c) show that $r_c$ decreases with increasing nonreciprocity $J_-$ and increases with increasing noise strength $T$, respectively. Thus stronger non-reciprocal rotation makes the homogeneous chiral state more locally fragile, whereas noise suppresses the growth of seeded defects and increases the perturbation size required to

trigger collapse.

The characteristic radius $r_c$ should not be interpreted as a thermodynamic nucleation barrier of a metastable phase. Rather, it is the minimal local perturbation size required to bypass the slow linear growth of the finite length scale instability and directly seed the nonlinear defect structures that destroy the homogeneous chiral background. In this sense, $r_c$ may be viewed as an estimate of the characteristic size beyond which the unstable finite-wavelength mode can directly trigger the breakdown of the chiral rotating state through a local perturbation.

## III. GLOBAL CHIRALITY AND FINITE-SIZE SCALING

This section provides supplementary details for the global chirality analysis. We first define the global chirality used throughout the microscopic analysis. We then present additional finite-size scaling data that support the collapse shown in Fig. 2(c). Finally, we give a simple geometric estimate for the crossover scale.

### A. Definition of the global chirality

The instantaneous global chirality is defined as the particle-averaged angular velocity,

$$\chi(t) = \frac{1}{N}\sum_{i=1}^{N}\chi_i(t), \tag{12}$$

with

$$\chi_i(t) = \sum_{\alpha\in\{A,B\}}\frac{J_{s_i\alpha}}{N_i^{\alpha}}\sum_{j\in\mathcal{N}_i^{\alpha}}\sin\big(\theta_j(t)-\theta_i(t)\big). \tag{13}$$

Thus, $\chi(t)$ measures the instantaneous collective rotation rate of the system. Long-time averages are denoted by an overbar, $\overline{X}$, in order to avoid confusion with the angle brackets used elsewhere for spatial averages.

### B. Additional finite-size scaling results

Figure 4 provides additional finite-size scaling results for the global chirality. For each run, $\overline{|\chi|}$ is obtained by averaging $|\chi(t)|$ over a late-time window after discarding the initial transient.

Panel (a) shows the system-size dependence of $\overline{|\chi|}$ for several values of $J_-$. For all couplings shown, the long-time chirality decreases systematically with increasing system size. At large $L$, the data are broadly consistent with the scaling $\overline{|\chi|} \sim L^{-1}$, as indicated by the dashed guide line. At fixed $L$, increasing $J_-$ yields a larger chirality, while decreasing $J_-$ shifts the crossover to larger system sizes.

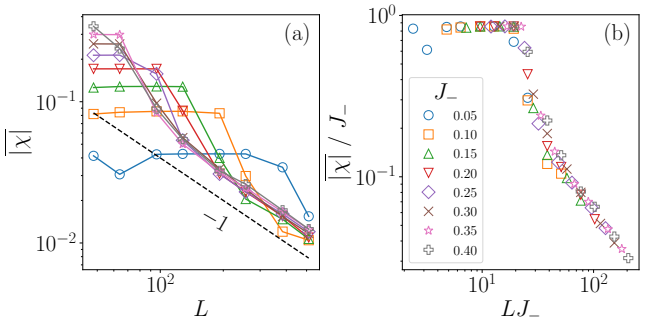


FIG. 4. Additional finite-size scaling results for the global chirality at fixed self-propulsion speed $v_0 = 5$. (a) Long-time average $\overline{|\chi|}$ as a function of the system size $L$. The dashed line indicates the guide-to-the-eye scaling $\overline{|\chi|} \sim L^{-1}$. (b) Rescaled plot of $\overline{|\chi|}/J_-$ versus $LJ_-$ for the same data. The approximate collapse is consistent with the finite-size scaling form $\overline{|\chi|} = J_-\mathcal{X}(LJ_-)$ at fixed $v_0$. In the main text, this collapse is generalized to the scaling variable $LJ_-/v_0$ when data with different self-propulsion speeds are combined.

Panel (b) replots the same data in the rescaled form $\overline{|\chi|}/J_-$ as a function of $LJ_-$. At fixed $v_0$, the approximate collapse onto a single master curve is consistent with the scaling form

$$\overline{|\chi|} = J_-\mathcal{X}(LJ_-). \tag{14}$$

In the small-$LJ_-$ regime, the rescaled chirality remains of order unity, consistent with an almost homogeneous rotating state. In the large-$LJ_-$ regime, the data cross over toward the asymptotic decay

$$\frac{\overline{|\chi|}}{J_-} \sim (LJ_-)^{-1}. \tag{15}$$

When data at different self-propulsion speeds are combined, the corresponding scaling variable becomes $LJ_-/v_0$, as discussed in the main text.

### C. Geometric estimate of the crossover scale

To motivate the crossover scale, we consider an idealized homogeneous rotating state on the antisymmetric line $J_+ = 0$, represented by one particle of each species starting from the same position with a constant phase lag

$$\Delta\phi = \theta_B - \theta_A. \tag{16}$$

In a spatially homogeneous state, the same-species contributions vanish identically, so the deterministic angular dynamics reduces to

$$\dot\theta_A = J_{AB}\sin\Delta\phi, \quad \dot\theta_B = -J_{BA}\sin\Delta\phi. \tag{17}$$

For $J_+ = 0$, one has

$$J_{AB} = J_-, \quad J_{BA} = -J_-, \tag{18}$$

and therefore

$$\dot{\theta}_A = \dot{\theta}_B \equiv \omega, \quad \omega = J_- \sin\Delta\phi. \tag{19}$$

The phase lag $\Delta\phi$ is then constant, and both particles execute uniform circular motion with the same angular frequency $\omega$.

The corresponding rotation radius is

$$r_{\rm rot} = \frac{v_0}{|\omega|} = \frac{v_0}{|J_- \sin\Delta\phi|}. \tag{20}$$

Choosing the initial conditions

$$\theta_A(0) = 0, \quad \theta_B(0) = \Delta\phi, \quad \boldsymbol{r}_A(0) = \boldsymbol{r}_B(0) = 0, \tag{21}$$

the particle trajectories can be written conveniently in complex notation, $z = x + iy$, as

$$z_A(t) = \frac{v_0}{i\omega}\big(e^{i\omega t} - 1\big), \quad z_B(t) = \frac{v_0}{i\omega} e^{i\Delta\phi}\big(e^{i\omega t} - 1\big). \tag{22}$$

Their relative displacement is therefore

$$z_B(t) - z_A(t) = \frac{v_0}{i\omega}\big(e^{i\Delta\phi} - 1\big)\big(e^{i\omega t} - 1\big), \tag{23}$$

which gives

$$d(t) \equiv |z_B(t) - z_A(t)| = 4r_{\rm rot}\left|\sin\frac{\Delta\phi}{2}\right|\left|\sin\frac{\omega t}{2}\right|. \tag{24}$$

The maximal separation attainable during the orbit is thus

$$d_{\max}(\Delta\phi) = 4r_{\rm rot}\left|\sin\frac{\Delta\phi}{2}\right|. \tag{25}$$

For the prepared homogeneous rotating state used in the stability measurements, the phase lag is

$$\Delta\phi = \frac{\pi}{2}, \tag{26}$$

and the maximal separation becomes

$$d_{\max} = 2\sqrt{2} r_{\rm rot}. \tag{27}$$

This directly yields the geometric estimate

$$L_c \sim 2\sqrt{2} r_{\rm rot}. \tag{28}$$

More generally, the numerical prefactor depends on the phase lag through $d_{\max}(\Delta\phi) = 4r_{\rm rot}|\sin(\Delta\phi/2)|$, so $2\sqrt{2}$ is not universal. Nevertheless, the crossover remains controlled by the orbit size of the ideal homogeneous rotating state, which explains why the finite-size scaling is naturally organized by the ratio of the system size to the intrinsic rotation scale.

## IV. STRUCTURE OF THE CHAOTIC STATE

This section collects the definitions and supplementary results underlying the characterization of the large-system chaotic state discussed in the main text. We first define the coarse-grained observables and then present the species-resolved real-space correlations and velocity spectra summarized in Fig. 5.

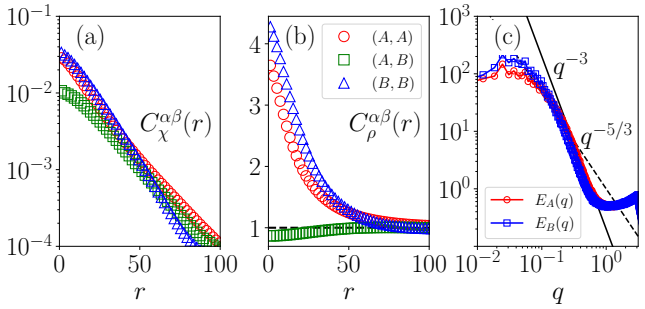


FIG. 5. Species-resolved structural observables in the chaotic regime. (a) Correlations of the coarse-grained chirality field for the three channels $(\alpha,\beta) = (A,A),(A,B),(B,B)$. (b) Correlations of the coarse-grained particle-number field for the same three channels. (c) Species-resolved velocity spectra $E_\alpha(q)$ obtained from the density-weighted coarse-grained velocity fields. The reference slopes $q^{-5/3}$ and $q^{-3}$ are shown for comparison only. Parameters: $J_- = 0.2$ and $L = 1024$.

### A. Coarse-grained fields

To characterize the chaotic state, we partition the system into square boxes of linear size $1 \times 1$ and construct species-resolved coarse-grained fields on this grid. For each species $\alpha \in \{A, B\}$, we define the coarse-grained particle-number field $\rho_\alpha(\boldsymbol{r}, t)$ as the number of particles of species $\alpha$ contained in the box centered at $\boldsymbol{r}$. Since the box size is unity, this coincides numerically with the corresponding coarse-grained density.

Using the same coarse-graining procedure, we define the coarse-grained chirality field $\chi_\alpha(\boldsymbol{r}, t)$ as the sum of the single-particle chiralities over all particles of species $\alpha$ in the same box. Likewise, we define the coarse-grained velocity field $\boldsymbol{v}_\alpha(\boldsymbol{r}, t) = \big(v_{x,\alpha}(\boldsymbol{r}, t), v_{y,\alpha}(\boldsymbol{r}, t)\big)$, where $v_{x,\alpha}$ and $v_{y,\alpha}$ are the sums of $\cos\theta_i$ and $\sin\theta_i$, respectively, over all particles of species $\alpha$ in the box. Thus, all coarse-grained observables are constructed from the same local box average, and both $\chi_\alpha$ and $\boldsymbol{v}_\alpha$ are density-weighted fields.

### B. Species-resolved real-space correlation functions and Velocity power spectra

We quantify the real-space structure through species-resolved disconnected correlation functions of the coarse-grained particle-number and chirality fields. For $X \in \{\rho, \chi\}$, we define

$$C_X^{\alpha\beta}(r) = \frac{\overline{\langle X_\alpha(\boldsymbol{r}_0, t) X_\beta(\boldsymbol{r}_0 + \boldsymbol{r}, t)\rangle_{\boldsymbol{r}_0, \hat{\boldsymbol{r}}}}}{\rho_0^2}, \tag{29}$$

where $\langle\cdots\rangle_{\boldsymbol{r}_0,\hat{\boldsymbol{r}}}$ denotes averaging over the box origin $\boldsymbol{r}_0$ and over the directions of $\boldsymbol{r}$ at fixed $r = |\boldsymbol{r}|$. The factor $\rho_0^2$ is included only as a common normalization.

To characterize the same state in Fourier space, we measure species-resolved velocity power spectra from the

coarse-grained velocity fields. For each snapshot, we compute the two-dimensional discrete Fourier transform $\hat{\boldsymbol{v}}_\alpha(\boldsymbol{q},t) = \big(\hat{v}_{x,\alpha}(\boldsymbol{q},t), \hat{v}_{y,\alpha}(\boldsymbol{q},t)\big)$, with the convention

$$\hat{v}_{\mu,\alpha}(\boldsymbol{q},t) = \frac{1}{L^2}\sum_{\boldsymbol{r}} v_{\mu,\alpha}(\boldsymbol{r},t)e^{-i\boldsymbol{q}\cdot\boldsymbol{r}}, \quad \mu \in \{x,y\}, \quad (30)$$

on the coarse-grained grid. The corresponding two-dimensional velocity power spectral density is then

$$E_\alpha^{(2D)}(\boldsymbol{q},t) = \frac{1}{2}\left(|\hat{v}_{x,\alpha}(\boldsymbol{q},t)|^2 + |\hat{v}_{y,\alpha}(\boldsymbol{q},t)|^2\right). \quad (31)$$

We then time-average $E_\alpha^{(2D)}(\boldsymbol{q},t)$ in the stationary regime and perform radial binning in wave-number space to obtain the one-dimensional spectrum $E_\alpha(q)$ with $q = |\boldsymbol{q}|$. Because the coarse-grained velocity field is density weighted, the spectra probe both orientational coherence and density modulation.

### C. Characteristics of the chaotic state

The chirality correlations $C_\chi^{\alpha\beta}(r)$ in Fig. 5(a) decay rapidly with distance in all channels, confirming the absence of long-range chiral order in the broken state. By contrast, the particle-number correlations $C_\rho^{\alpha\beta}(r)$ in Fig. 5(b) remain strongly channel dependent: the intra-species correlations exhibit a pronounced short-range enhancement, while the inter-species correlation is suppressed at short distances. This difference reflects the tendency of the chaotic state to form locally species-segregated clustered structures.

The velocity spectra shown in Fig. 5(c) are broadly distributed in wave number for both species and do not exhibit a sharp selected peak. The reference slopes $q^{-5/3}$ and $q^{-3}$ are included only for comparison: the former as the canonical benchmark from classical turbulence [3, 4], and the latter as a guide to the steeper decay visible in the present data. The spectra do not display a clear power-law regime over an extended wave-number range, but they remain broad, reminiscent of the broad spectra often reported in active turbulence [5, 6].

Taken together, these results show that the large-system steady state combines short-ranged chiral correlations, channel-dependent clustered density structure, and broad spectral support, consistent with a spatially extended chaotic regime [7].

## V. COMPARISON WITH FRUCHART *ET AL.*

This section clarifies the normalization convention used in the microscopic dynamics and its relation to the finite-size scaling. We first compare the normalized torque convention adopted in this work with the unnormalized convention used in Ref. [2], and show how the corresponding scaling variable is modified. We then revisit the parameter choice used in Ref. [2] in our notation.

### A. Normalization convention in the torque term

In the microscopic model used in the main text, the alignment torque generated by neighbors of each species is normalized separately by the local neighbor number $N_i^\alpha$. This yields the angular dynamics

$$\dot{\theta}_i = \sum_{\alpha\in\{A,B\}} \frac{J_{s_i\alpha}}{N_i^\alpha} \sum_{j\in\mathcal{N}_i^\alpha} \sin(\theta_j - \theta_i) + \sqrt{2T}\xi_i(t). \quad (32)$$

This convention avoids an artificial mixing of couplings: if the torque were normalized by the total number of neighbors across both species, then the interaction with one species would depend implicitly on the local density of the other, even when the corresponding coupling vanishes.

For comparison, we also checked the unnormalized variant used in Ref. [2],

$$\dot{\theta}_i = \sum_{j\in\mathcal{N}_i} J_{s_i s_j} \sin(\theta_j - \theta_i) + \sqrt{2T}\xi_i(t), \quad (33)$$

where the torque is not divided by the local neighbor number. In this convention, the characteristic angular-velocity scale is proportional not only to the coupling but also to the typical number of interacting neighbors, and therefore acquires an additional factor of order $\rho_0\pi R^2$, with $\rho_0 = \rho_A = \rho_B$. Correspondingly, the natural finite-size scaling variable is controlled by

$$\frac{L\rho_0\pi R^2|J_-|}{v_0}, \quad (34)$$

rather than by $L|J_-|/v_0$ alone.

Consistent with this expectation, the finite-size scaling of the global chirality remains qualitatively similar in the unnormalized model, but the rescaled variables acquire an additional geometric factor. Figure 6 shows the corresponding scaling plots. Here $R = 1$, so the geometric factor reduces to $\rho_0\pi$. At fixed $v_0$, $\rho_0$, and $R$, the data are reasonably organized by $LJ_-$, as shown in Fig. 6(a). A broader collapse across different self-propulsion speeds is obtained by using the variable $L\rho_0\pi J_-/v_0$, as shown in Fig. 6(b). The collapse is less accurate than in the normalized convention used in the main text, especially at small $v_0$, but the same qualitative conclusion holds: the global chirality decreases systematically with system size, and the apparently homogeneous chiral state becomes unstable in the thermodynamic limit.

### B. Revisiting the parameter choice used by Fruchart *et al.*

This distinction is especially important when comparing our results with the microscopic simulations of Fruchart *et al.* [2], where the unnormalized convention of Eq. (33) was used. In their supplemental material,

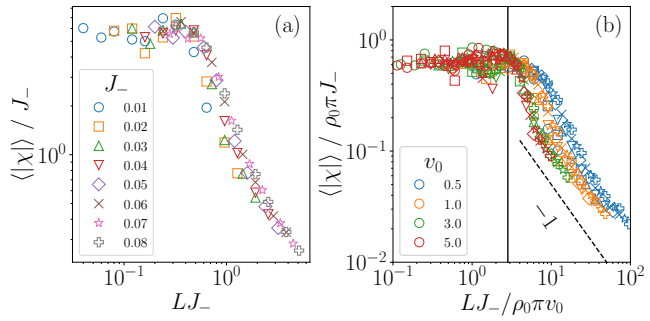


FIG. 6. Finite-size scaling of the global chirality in the unnormalized microscopic convention of Eq. (33). (a) $\overline{|\chi|}/J_-$ versus $LJ_-$ at fixed $v_0 = 1$. (b) $\overline{|\chi|}/(\rho_0\pi J_-)$ versus $L\rho_0\pi J_-/v_0$ for several values of $v_0$.

the representative parameter choice illustrating a microscopic homogeneous chiral phase corresponds, in the notation of the present work, to

$$L_x = L_y = 8, R = 2, v_0 = \frac{1}{2}, \rho_A = \rho_B = 4, T = 0.02,$$

with interaction matrix

$$J_{\alpha\beta} = \begin{pmatrix} 0.39 & -0.0975 \\ 0.0975 & 0.39 \end{pmatrix}.$$

To compare this parameter set directly with the one used in the main text, we rescale space and time according to

$$\tilde{\boldsymbol{r}} = l\boldsymbol{r}, \tilde{t} = ut, \tag{35}$$

so that the equations of motion preserve their form provided

$$\begin{aligned} \tilde{L} = lL, \tilde{R} = lR, \tilde{v}_0 = \frac{l}{u}v_0, \\ \tilde{\rho}_\alpha = \frac{\rho_\alpha}{l^2}, \tilde{T} = \frac{T}{u}, \tilde{J}_{\alpha\beta} = \frac{J_{\alpha\beta}}{u}. \end{aligned} \tag{36}$$

Choosing

$$l = \frac{1}{R} = \frac{1}{2}, u = \frac{2v_0}{R}, \tag{37}$$

gives the rescaled parameters

$$L_x = L_y = 4, R = 1, v_0 = \frac{1}{2}, \rho_A = \rho_B = 16, T = 0.04,$$

and

$$J_{\alpha\beta} = \begin{pmatrix} 0.78 & -0.195 \\ 0.195 & 0.78 \end{pmatrix}.$$

In our notation, this corresponds to

$$J_+ = 0, J_- = -0.195.$$

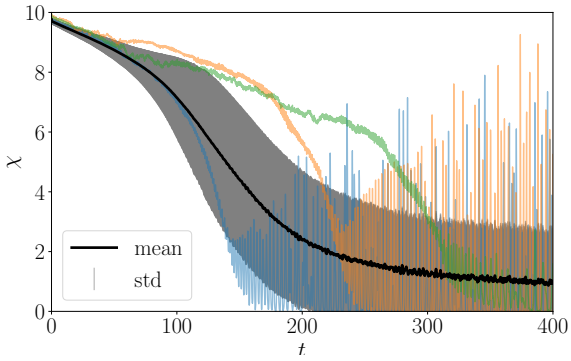


FIG. 7. Global chirality for the rescaled parameter choice corresponding to Ref. [2] in the unnormalized microscopic convention. Thin colored curves: individual realizations. Thick black curve: ensemble mean. Shaded region: standard deviation.

Thus, up to the sign convention fixed by the species labeling, this parameter choice lies exactly on the purely antisymmetric line discussed in the main text.

In the unnormalized convention of Eq. (33), the relevant finite-size variable is enhanced by the typical number of interacting neighbors. For the rescaled parameter set above, one finds

$$\frac{L\rho_0\pi|J_-|}{v_0} = \frac{4 \times 16 \times \pi \times 0.195}{0.5} \simeq 78.4,$$

which is far larger than the geometric crossover value $2\sqrt{2} \simeq 2.83$. Equivalently, although $L = 4$, the rotation radius in the unnormalized convention is much smaller than the box size, so $L/r_{\rm rot} \gg 1$.

For this rescaled parameter choice, we measure the global chirality as the particle-averaged deterministic angular velocity

$$\chi = \frac{1}{N}\sum_{i=1}^{N}\sum_{j\in\mathcal{N}_i} J_{s_i s_j}\sin(\theta_j - \theta_i), \tag{38}$$

with the noise term excluded. Figure 7 shows the corresponding time evolution of $\chi(t)$. The thin colored curves denote individual realizations, while the thick black curve and shaded region show the ensemble mean and standard deviation obtained from 800 independent simulation runs. Although the chirality remains finite for a substantial transient, the ensemble mean decreases over time and the fluctuations broaden, indicating that even this parameter regime does not support a stable homogeneous rotating state.

The observation window used in Ref. [2] is finite $t < 40$, and therefore probes only the transient regime. Thus, even for the parameter regime originally used to illustrate microscopic chiral order, the chiral state is better interpreted as a long-lived but finite-size transient.

## VI. NUMERICAL INTEGRATION

For the microscopic model, the stochastic equations of motion are integrated using the Euler–Maruyama method. The integration time step is set to $\Delta t = 0.1$ throughout, except for the unnormalized microscopic convention of Eq. (33), where we use $\Delta t = 0.01$. We also verified that using even smaller time steps yields almost identical results, confirming that our observations are numerically stable and robust against the choice of temporal discretization.

## VII. BOLTZMANN KINETIC THEORY FOR THE TWO-SPECIES NON-RECIPROCAL VICSEK MODEL

This section provides the kinetic description used in the main text to connect the microscopic non-reciprocal Vicsek dynamics to a continuum theory that still retains the orientational dynamics explicitly. Our starting point is a dilute two-species Vicsek-type model with constant self-propulsion speed $v_0$, binary alignment interactions, and angular noise. The kinetic theory follows the standard Boltzmann logic developed for aligning active particles [8, 9], with nonreciprocity encoded through species-dependent scattering rules and collision rates.

### A. One-particle distribution and Boltzmann equation

For each species $\alpha \in \{A, B\}$, we introduce a one-particle distribution function $f^\alpha(\boldsymbol{r}, \theta, t)$ such that $f^\alpha(\boldsymbol{r}, \theta, t) d^2r d\theta$ is the expected number of particles of species $\alpha$ in the phase-space element $(\boldsymbol{r}, \boldsymbol{r} + d\boldsymbol{r}) \times (\theta, \theta + d\theta)$ at time $t$. Between interaction events, particles move ballistically with velocity $v_0 \hat{\boldsymbol{e}}(\theta)$, where $\hat{\boldsymbol{e}}(\theta) = (\cos\theta, \sin\theta)$.

Under the assumptions of dilute binary collisions and molecular chaos, the distribution obeys

$$\partial_t f^\alpha + v_0 \hat{\boldsymbol{e}}(\theta) \cdot \nabla f^\alpha = I_{\mathrm{sd}}[f^\alpha] + \sum_{\beta \in \{A,B\}} I_{\mathrm{coll}}[f^\alpha, f^\beta]. \quad (39)$$

Here $I_{\mathrm{sd}}$ describes angular self-diffusion and $I_{\mathrm{coll}}$ binary alignment interactions between species $\alpha$ and $\beta$.

We model self-diffusion as a Poisson process of rate $\lambda$ in which a particle changes its orientation by a random increment drawn from a wrapped Gaussian $P_\eta(\phi)$ of variance $\eta^2$,

$$I_{\mathrm{sd}}[f](\boldsymbol{r}, \theta, t) = -\lambda f(\boldsymbol{r}, \theta, t) + \lambda \int_{-\pi}^{\pi} d\theta' f(\boldsymbol{r}, \theta', t) P_\eta(\theta - \theta'). \quad (40)$$

The wrapped Gaussian is

$$P_\eta(\phi) = \frac{1}{\sqrt{2\pi\eta^2}} \sum_{m=-\infty}^{\infty} \exp\left[-\frac{(\phi - 2\pi m)^2}{2\eta^2}\right]. \quad (41)$$

The collision term is written in gain–loss form. Consider a particle of species $\alpha$ with pre-collision angle $\theta_1$ interacting with a particle of species $\beta$ at angle $\theta_2$, and define the relative angle $\phi = \theta_2 - \theta_1 \in (-\pi, \pi]$. A collision occurs with rate $K^{\alpha\beta}(\theta_1, \theta_2)$, and the post-collision orientation of the first particle is taken to be

$$\theta = \theta_1 + H^{\alpha\beta}(\phi) + \xi,$$

where $H^{\alpha\beta}(\phi)$ is the deterministic scattering angle and $\xi$ is an independent random increment drawn from $P_\eta$. With these conventions,

$$\begin{aligned} I_{\mathrm{coll}}[f^\alpha, f^\beta](\boldsymbol{r}, \theta, t) = & -f^\alpha(\boldsymbol{r}, \theta, t) \int_{-\pi}^{\pi} d\theta' K^{\alpha\beta}(\theta, \theta') f^\beta(\boldsymbol{r}, \theta', t) \\ & + \int_{-\pi}^{\pi} d\theta_1 \int_{-\pi}^{\pi} d\theta_2 f^\alpha(\boldsymbol{r}, \theta_1, t) f^\beta(\boldsymbol{r}, \theta_2, t) K^{\alpha\beta}(\theta_1, \theta_2) P_\eta\big(\theta - \theta_1 - H^{\alpha\beta}(\theta_2 - \theta_1)\big). \end{aligned} \quad (42)$$

For metric interactions with species-dependent cross section $2r_0^{\alpha\beta}$, the scattering rate is the product of cross section and relative speed. Since all particles move at speed $v_0$,

$$\begin{aligned} K^{\alpha\beta}(\theta_1, \theta_2) &= 2 r_0^{\alpha\beta} v_0 \left| \hat{\boldsymbol{e}}(\theta_2) - \hat{\boldsymbol{e}}(\theta_1) \right| \\ &= 4 r_0^{\alpha\beta} v_0 \left| \sin\left(\frac{\phi}{2}\right) \right|. \end{aligned} \quad (43)$$

Nonreciprocity enters through the species dependence of both $r_0^{\alpha\beta}$ and the scattering rule $H^{\alpha\beta}(\phi)$. In the model studied here, all interactions are polar-aligning except the asymmetric interspecies channel in which species $B$ tends to anti-align with $A$, whereas species $A$ aligns with $B$. We therefore choose

$$H^{\alpha\beta}(\phi) = \begin{cases} H^A(\phi) \equiv \dfrac{\phi + \pi \ (\mathrm{mod}\ 2\pi)}{2}, & \alpha = B,\ \beta = A, \\ H^{\mathrm{F}}(\phi) \equiv \dfrac{\phi}{2}, & \text{otherwise.} \end{cases} \quad (44)$$

with the $(\mathrm{mod}\, 2\pi)$ convention chosen such that $H^A(\phi) \in [-\pi/2, \pi/2]$ for $\phi \in (-\pi, \pi]$.

### B. Nondimensionalization and angular Fourier decomposition

It is convenient to rescale time by $\lambda^{-1}$, length by $v_0/\lambda$, and density by the mean total density $\rho_0$. Writing $\tilde{t} = \lambda t$, $\tilde{\boldsymbol{r}} = (\lambda/v_0)\boldsymbol{r}$, and $\tilde{f}^\alpha = f^\alpha/\rho_0$, Eq. (39) keeps its form with $v_0 = \lambda = \rho_0 = 1$. In the following we drop tildes and work in these dimensionless units.

In two dimensions we use complex coordinates $z = x + iy$ and $z^* = x - iy$, with derivatives $\partial_z = (\partial_x - i\partial_y)/2$ and $\partial_{z^*} = (\partial_x + i\partial_y)/2$, so that

$$\hat{\boldsymbol{e}}(\theta)\cdot\nabla = e^{i\theta}\partial_z + e^{-i\theta}\partial_{z^*}. \tag{45}$$

We then expand the one-particle distribution in angular Fourier modes,

$$f^\alpha(\boldsymbol{r},\theta,t) = \frac{1}{2\pi}\sum_{k=-\infty}^{\infty} f_k^\alpha(\boldsymbol{r},t)e^{-ik\theta}. \tag{46}$$

Since $f^\alpha$ is real, the modes satisfy $f_{-k}^\alpha = (f_k^\alpha)^*$. The monopole $f_0^\alpha$ is the density field $\rho^\alpha$, while the dipole $f_1^\alpha = m_x^\alpha + i m_y^\alpha$ is the complex polarization field.

Projecting Eq. (39) onto the angular harmonics yields a coupled hierarchy for the modes. The self-diffusion operator is diagonal in Fourier space,

$$\int_{-\pi}^{\pi} d\theta e^{ik\theta} I_{\mathrm{sd}}[f^\alpha] = -(1-P_k)f_k^\alpha, \tag{47}$$

with

$$P_k = \int_{-\pi}^{\pi} d\phi P_\eta(\phi)e^{ik\phi} = \exp\left(-\frac{\eta^2 k^2}{2}\right).$$

Writing the collision rate in terms of the dimensionless coupling

$$K^{\alpha\beta}(\phi) = 2\pi\kappa^{\alpha\beta}\left|\sin\left(\frac{\phi}{2}\right)\right|, \quad \kappa^{\alpha\beta} = \frac{2r_0^{\alpha\beta}\rho_0 v_0}{\pi\lambda}, \tag{48}$$

the mode hierarchy becomes

$$\begin{aligned}&\partial_t f_k^\alpha + \left(\partial_{z^*} f_{k-1}^\alpha + \partial_z f_{k+1}^\alpha\right)\\ &\quad = -(1-P_k)f_k^\alpha + \sum_\beta\sum_{l=-\infty}^{\infty}\kappa^{\alpha\beta}J_{k,l}^{\alpha\beta}f_{k-l}^\alpha f_l^\beta.\end{aligned} \tag{49}$$

The coefficients are

$$J_{k,l}^{\alpha\beta} = P_k L_{k,l}^{\alpha\beta} - I_l, \tag{50}$$

with

$$L_{k,l}^{\alpha\beta} = \int_{-\pi}^{\pi} d\phi\left|\sin\left(\frac{\phi}{2}\right)\right|\exp\left[ikH^{\alpha\beta}(\phi) - il\phi\right], \tag{51}$$

$$I_m = \int_{-\pi}^{\pi} d\phi\left|\sin\left(\frac{\phi}{2}\right)\right|e^{im\phi}. \tag{52}$$

For integer $m$, the latter evaluates to

$$I_m = \frac{4}{1-4m^2}. \tag{53}$$

For the forward-aligning channel $H^{\mathrm{F}}(\phi) = \phi/2$ one obtains

$$L_{k,l}^{\mathrm{F}} = I_{k/2-l}, \tag{54}$$

whereas for the asymmetric anti-aligning channel one finds

$$L_{k,l}^{\mathrm{A}} = \begin{cases}(-1)^m\dfrac{4}{1-(k-2l)^2}, & k = 2m,\\ (-1)^m\pi\left(\delta_{l,m} - \delta_{l,m+1}\right), & k = 2m+1.\end{cases} \tag{55}$$

The channel dependence can be summarized as

$$\boldsymbol{L}_{k,l} = \begin{pmatrix}L_{k,l}^{\mathrm{F}} & L_{k,l}^{\mathrm{F}}\\ L_{k,l}^{\mathrm{A}} & L_{k,l}^{\mathrm{F}}\end{pmatrix}, \tag{56}$$

where the species ordering is $(A, B)$.

In the notation used in the main text, we fix the intraspecies couplings to $\kappa^{AA} = \kappa^{BB} \equiv \kappa_0$ and take symmetric interspecies collision rates $\kappa^{AB} = \kappa^{BA} \equiv \kappa$, so that the nonreciprocity is carried entirely by the asymmetric scattering rule.

Equation (49) preserves global rotational invariance. Under $\theta \to \theta + \theta_0$ one has $f_k^\alpha \to e^{ik\theta_0}f_k^\alpha$, while $z \to e^{i\theta_0}z$ and $z^* \to e^{-i\theta_0}z^*$, which leaves the hierarchy invariant. In numerical implementations, the infinite hierarchy of angular modes must nevertheless be truncated at a finite order. We therefore set $f_k^\alpha = 0$ for $|k| > k_m$, with the specific choice of $k_m$ reported in Sec. XI.

### C. Linear stability of the spatially homogeneous disordered state

To determine the onset of homogeneous chiral order, we first analyze the stability of the spatially homogeneous disordered state,

$$f_k^\alpha = \delta_{k,0},$$

for both species. Neglecting spatial gradients and perturbing the disordered state as

$$f_k^\alpha = \delta_{k,0} + (1-\delta_{k,0})\epsilon_k^\alpha, \quad |\epsilon_k^\alpha| \ll 1,$$

we substitute into Eq. (49) and keep only linear terms. This gives

$$\dot{\epsilon}_k^\alpha = -(1-P_k)\epsilon_k^\alpha + \sum_{\beta\in\{A,B\}}\kappa^{\alpha\beta}\left(J_{k,0}^{\alpha\beta}\epsilon_k^\alpha + J_{k,k}^{\alpha\beta}\epsilon_k^\beta\right) + \mathcal{O}(\epsilon^2). \tag{57}$$

Each angular harmonic therefore decouples, and for every $k \geq 1$ the problem reduces to a $2\times 2$ linear system,

$$\partial_t\begin{pmatrix}\epsilon_k^A\\ \epsilon_k^B\end{pmatrix} = \boldsymbol{M}_k\begin{pmatrix}\epsilon_k^A\\ \epsilon_k^B\end{pmatrix}, \tag{58}$$

where

$$\boldsymbol{M}_k = \begin{pmatrix} P_k - 1 + \kappa^{AA} J^{AA}_{k,0} + \kappa^{AA} J^{AA}_{k,k} + \kappa^{AB} J^{AB}_{k,0} & \kappa^{AB} J^{AB}_{k,k} \\ \kappa^{BA} J^{BA}_{k,k} & P_k - 1 + \kappa^{BB} J^{BB}_{k,0} + \kappa^{BB} J^{BB}_{k,k} + \kappa^{BA} J^{BA}_{k,0} \end{pmatrix}. \tag{59}$$

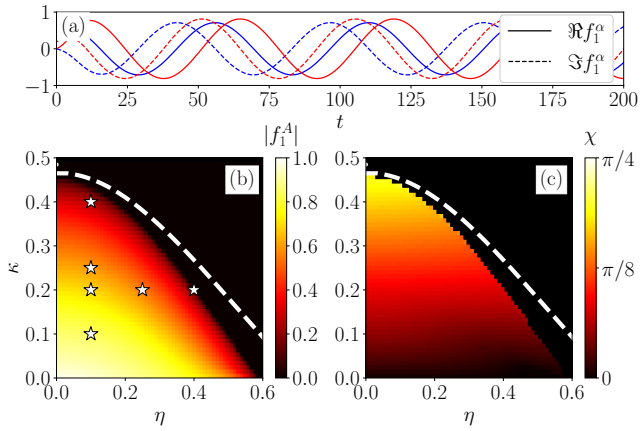


FIG. 8. Spatially homogeneous dynamics of the truncated Boltzmann hierarchy and comparison with linear stability. (a) Representative time series of the polarization mode $f_1^\alpha(t)$ in the spatially homogeneous truncated hierarchy ($k_m = 50$) at $\kappa_0 = 0.5$, $\kappa = 0.1$, and $\eta = 0.3$. (b) Steady-state polarization magnitude $|f_1^A|$. (c) Mean chirality $\chi = 2\pi/\mathcal{T}$. The white dashed lines mark the linear-stability boundary of the disordered state determined by the condition $a_1 = 0$ for the $k = 1$ eigenvalue of $\boldsymbol{M}_1$.

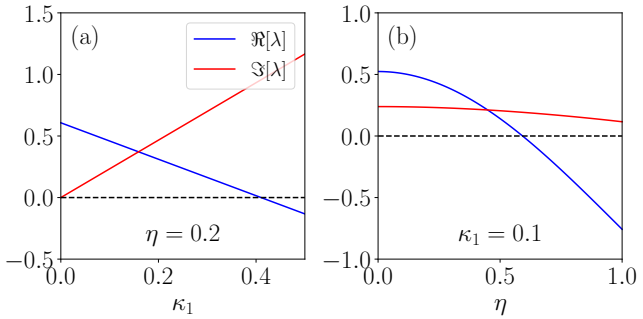


FIG. 9. Eigenvalues of the linearized matrix $\boldsymbol{M}_1$ for the first harmonic. (a) Real and imaginary parts, $a_1$ and $b_1$, as functions of the interspecies coupling $\kappa$. (b) $a_1$ and $b_1$ as functions of the noise amplitude $\eta$. The sign change of $a_1$ determines the stability boundary of the disordered state, while $b_1$ fixes the rotation rate at onset and depends primarily on the nonreciprocal coupling.

Because $\boldsymbol{M}_k$ is real, its eigenvalues appear in complex-conjugate pairs, $\lambda_k^{\pm} = a_k \pm i b_k$. The first harmonic $k = 1$ governs the onset of the homogeneous chiral dynamics: the real part $a_1$ determines the stability threshold of the disordered state, while the imaginary part $b_1$ sets the rotation frequency at onset.

As shown in Fig. 8(a), the spatially homogeneous truncated hierarchy reproduces a chiral rotating state in which the complex polarization approaches a stable limit cycle with well-defined period $\mathcal{T}$. Figures 8(b) and (c) show the corresponding phase diagrams for the steady-state polarization magnitude and the mean chirality in the $(\kappa, \eta)$ plane. The dashed white curves agree with the onset condition $a_1 = 0$ obtained from the linear stability analysis of the disordered state.

Figure 9 provides the complementary view in terms of the eigenvalues of $\boldsymbol{M}_1$. Increasing $\kappa$ drives $a_1$ through zero into the unstable regime, while $b_1$ grows approximately linearly with $\kappa$, consistent with the observed dependence of the rotation rate on nonreciprocity. In contrast, increasing the noise $\eta$ primarily lowers $a_1$, stabilizing the disordered state, while leaving $b_1$ only weakly affected.

## VIII. FLOQUET STABILITY ANALYSIS BY POWER ITERATION

In this section, we explain the iterative Floquet power method leading to the Floquet exponents shown in Fig. 4(a) in the main text. First, we present numerical evidence that an inhomogeneous perturbation breaks the homogeneous time-periodic chiral state in Sec. VIII A. Then, we introduce a Floquet analysis method which is suitable for a stability analysis of time-periodic states [10]. The numerical analysis from the Floquet analysis reveals a mode-selection mechanism for instability, which is presented in the main text.

### A. Instability against position-dependent perturbation

Figure 10 presents the time evolution of the homogeneous chiral state perturbed with a $\boldsymbol{r}$-dependent noise following the Boltzmann equation. The initially uniform state develops spatial modulations that subsequently amplify and drive the system into a dynamic state with spatially and temporally irregular patterns. This provides a direct kinetic-level example of the breakdown of homogeneous chiral order due to spatial fluctuations.

### B. Schematic description of the iterative Floquet power method

The numerical results in Fig. 10 establish the existence of the breakdown in the context of the kinetic theory. We now perform a quantitative linear stability analysis. Since the homogeneous chiral state is time-dependent, we adopt a Floquet method [10] for its stability analysis.

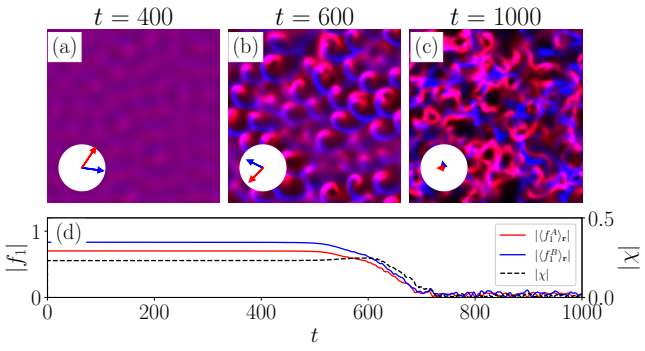


FIG. 10. Time evolution from a homogeneous chiral state perturbed with a weak $\boldsymbol{r}$-dependent noise following the kinetic Boltzmann equation. (a)–(c) Snapshots of the density field at successive times. The arrows in the inset indicate the mean polarizations of each species. (d) Time series of the absolute values of the mean polarization for both species (red and blue lines) and the global chirality $\chi = \left\langle f_0^\alpha \,\mathrm{Im}\left(f_1^{\alpha *} f_1^\alpha\right)/|f_1^\alpha|^2\right\rangle_{\boldsymbol{r},\alpha}$ (dashed line). Parameters: $\eta = 0.1$, $\kappa = 0.2$, and $L = 128$.

We work in the spatial Fourier space labeled by a wave vector $\boldsymbol{q}$ and denote the entire set of modes by $F(t) \equiv \left\{\hat{f}_k^\alpha(\boldsymbol{q},t)\right\}$, where

$$\hat{f}_k^\alpha(\boldsymbol{q},t) = \int d^2r f_k^\alpha(\boldsymbol{r},t)e^{-i\boldsymbol{q}\cdot\boldsymbol{r}}. \tag{60}$$

The Floquet analysis is performed around the homogeneous chiral state solution, which is obtained from the truncated Boltzmann equation restricted to the homogeneous manifold. This state will be called a reference state and denoted by $F_0(t) = \left\{\hat{f}_{k,0}^\alpha(\boldsymbol{q},t)\right\}$. It is a time-periodic state with period $\mathcal{T}$, and has support only at $\boldsymbol{q} = \boldsymbol{0}$.

We perturb the reference state at time $t = 0$ by assigning random numbers to all modes with $\boldsymbol{q} \neq \boldsymbol{0}$. The perturbed state $F(t)$ deviates from the reference state $F_0(t)$. We denote a deviation by $\delta F(t) = \{\delta f_k^\alpha(t)\}$ with $\delta f_k^\alpha(\boldsymbol{q},t) \equiv \hat{f}_k^\alpha(\boldsymbol{q},t) - \hat{f}_{k,0}^\alpha(\boldsymbol{q},t)$. In short, we will write $F(t) = F_0(t) + \delta F(t)$ or $\delta F(t) = F(t) - F_0(t)$.

The amplitude of an unstable mode grows exponentially in time. However, because of the time-periodic nature of the reference state, an exponential growth is superimposed with a time-periodic oscillation. To get rid of an influence from such an oscillatory behavior, we will measure the deviation $\delta F(t)$ only at discrete times $t_n = n\mathcal{T}$, integer multiples of $\mathcal{T}$. This is the key idea of the Floquet analysis. We also rescale the deviation $\delta F(t)$ at times $t_n$ to keep track of unstable modes over a long time span. The Floquet method combined with the rescaling will be called the iterative Floquet power method.

The Floquet power method starts by preparing for an initial state $F(0) = F_0(0) + \delta F(0)$, where a magnitude of $\delta F(0)$ is set to a target value $A_{\rm tar}$ taken to be small. A magnitude of $\delta F$ will be defined in the subsequent sections. Then, we repeat the following steps iteratively:

1. time evolution from $F(t_n)$ to $F(t_{n+1}^-)$
2. resetting the system in the homogeneous ($\boldsymbol{q} = 0$) sector to the reference orbit, $\delta f_k^\alpha(\boldsymbol{q} = 0, t_{n+1}) = 0$
3. rescaling of $\delta F(t_{n+1}^-)$ to $\delta F(t_{n+1})$ to make its magnitude to a target value $A_{\rm tar}$. In this step, one obtains a growth rate $\Lambda_n$ over the $n$th cycle.
4. preparation of $F(t_{n+1}) = F_0(t_{n+1}) + \delta F(t_{n+1})$ for the next iteration

Repeating this procedure yields a sequence of growth rates $\{\Lambda_n\}$, whose late-time average defines the corresponding Floquet exponent. In the rescaling step, one may rescale $\delta F$ locally at each $\boldsymbol{q}$ with a different rescale factor or globally with a common rescale factor, which results in a $\boldsymbol{q}$-dependent Floquet exponent or a global Floquet exponent, respectively. These two different methods are explained in the following subsections.

### C. Local Floquet exponent

The reference state $F_0(t)$ has support only at $\boldsymbol{q} = 0$. Thus, the quadratic term in the Boltzmann equation couples a nonzero $\boldsymbol{q}$ mode only to the reference mode in the leading linear order in $A_{\rm tar}$. Couplings between nonzero $\boldsymbol{q}$ modes are quadratic in $A_{\rm tar}$, which can be negligible in the linear stability analysis. Consequently, we can rescale each nonzero $\boldsymbol{q}$ mode independently to obtain the spectrum of Floquet exponents $\{\Lambda(\boldsymbol{q})\}$.

For a fixed nonzero wave vector $\boldsymbol{q}$, we define the magnitude of the corresponding mode as

$$|\delta F(t)|_{\boldsymbol{q}} := \left[\sum_{\alpha,k}\left|\delta f_k^\alpha(\boldsymbol{q},t)\right|^2\right]^{1/2}. \tag{61}$$

Note that the modes obey the Hermitian constraint $\hat{f}_k^\alpha(-\boldsymbol{q},t) = \hat{f}_{-k}^{\alpha *}(\boldsymbol{q},t)$. So, we rescale the modes at $\boldsymbol{q}$ and $-\boldsymbol{q}$ simultaneously as

$$\delta_k^\alpha(\pm\boldsymbol{q},t_{n+1}) = \frac{A_{\rm tar}}{r_n(\boldsymbol{q})}\delta_k^\alpha(\pm\boldsymbol{q},t_{n+1}^-) \tag{62}$$

with $\boldsymbol{q}$-dependent rescale factor

$$r_n(\boldsymbol{q}) = \sqrt{|\delta F(t_{n+1}^-)|_{\boldsymbol{q}}^2 + |\delta F(t_{n+1}^-)|_{-\boldsymbol{q}}^2}. \tag{63}$$

The iteration yields a sequence of one-cycle growth rates

$$\Lambda_n(\boldsymbol{q}) = \frac{1}{\mathcal{T}}\ln\left(\frac{r_n(\boldsymbol{q})}{A_{\rm tar}}\right). \tag{64}$$

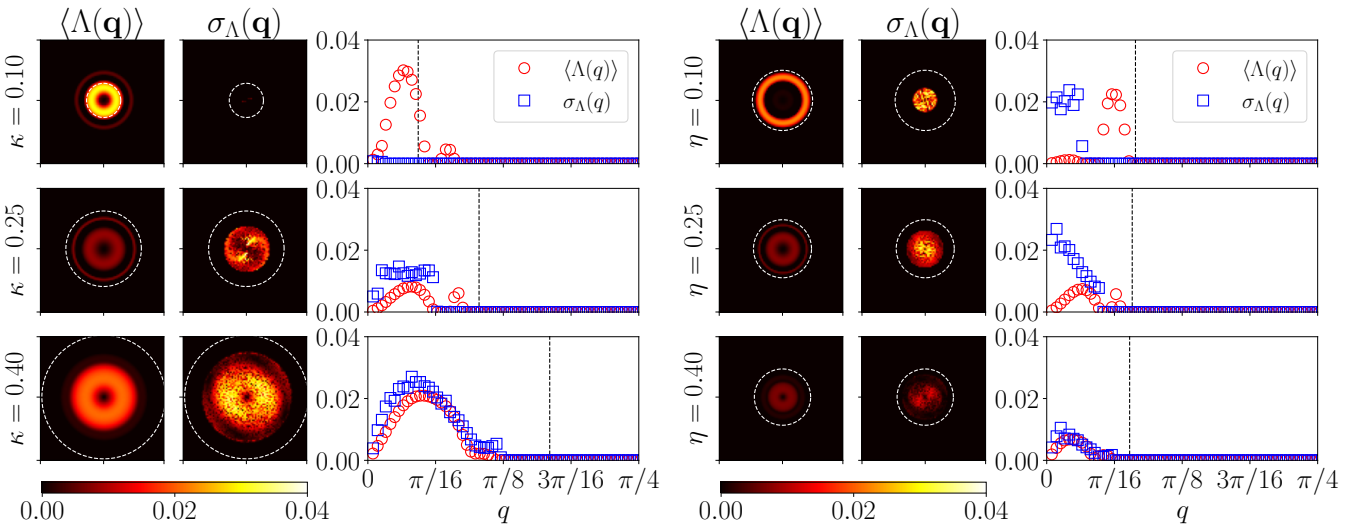


FIG. 11. Local Floquet spectrum obtained via paired-local normalization. Left half: dependence on $\kappa$ at fixed $\eta = 0.1$. Right half: dependence on $\eta$ at fixed $\kappa = 0.2$. In each row, the first two panels show two-dimensional maps of the local Floquet exponent $\Lambda(\boldsymbol{q})$ and its standard deviation $\sigma_\Lambda(\boldsymbol{q})$, and the rightmost panel shows the corresponding radial profiles as functions of $q = |\boldsymbol{q}|$. The white dashed ellipse in the two-dimensional plots and the black vertical dashed line in the radial profiles indicate the characteristic wave number $q_{\rm rot}$ of the homogeneous rotating cycle.

Discarding initial transient elements, we estimate the local Floquet exponent $\Lambda(\boldsymbol{q})$ as the average and its statistical uncertainty as the standard deviation $\sigma_\Lambda(\boldsymbol{q})$ of the sequence.

Figure 11 shows the resulting local Floquet spectrum. At weak nonreciprocity, for example $\kappa = 0.10$ and $\eta = 0.1$, the local exponent $\Lambda(\boldsymbol{q})$ exhibits a narrow annulus of unstable modes at $|\boldsymbol{q}| \approx q_{\rm rot}$, where

$$q_{\rm rot} := 2\pi\chi = \frac{2\pi}{r_{\rm rot}}, \tag{65}$$

is a characteristic wave number of the reference state characterized by the chirality $\chi$ and the radius of a chiral orbit $r_{\rm rot} = v_0/\chi$ with $v_0 = 1$ in the dimensionless unit. The corresponding standard deviation remains small. In this regime, the instability is controlled by a finite-$q$ band set by the rotation scale of the homogeneous cycle.

At intermediate nonreciprocity, around $\kappa = 0.25$, the ring near $q_{\rm rot}$ remains visible, but an additional unstable branch appears at smaller $q$. At the same time, $\sigma_\Lambda(\boldsymbol{q})$ increases in the unstable region, indicating competition between the finite-$q$ ring near $q_{\rm rot}$ and a lower-$q$ branch.

At stronger nonreciprocity, for example $\kappa = 0.40$, the lower-$q$ branch becomes dominant and the unstable region broadens. The corresponding shift toward longer wavelengths is consistent with the broader labyrinthine modulations that emerge in the unrestricted global power iteration discussed below.

The $\eta$ scan at fixed $\kappa = 0.2$ shows a different trend. As the noise amplitude is increased from $\eta = 0.1$ to 0.4, the unstable annulus remains concentrated near a finite wave number of order $q_{\rm rot}$, while its growth rate decreases and the unstable band narrows.

### D. Global Floquet exponent

Complementary to the $\boldsymbol{q}$-resolved Floquet spectrum $\Lambda(\boldsymbol{q})$, we evaluate a global Floquet exponent by adopting a rescaling method in which all modes of $\delta F(t)$ are rescaled by the same factor using a global magnitude

$$|\delta F(t)|_g = \frac{\Delta_x \Delta_y}{L_x L_y} \left[ \sum_{\alpha,k,\boldsymbol{q}} |\delta F(t)|^2_{\boldsymbol{q}} \right]^{1/2}, \tag{66}$$

where $\Delta_x$ and $\Delta_y$ are the grid spacings in the $x$ and $y$ directions, respectively (see Sec. XI).

For the global Floquet exponent, in each iteration, we rescale all the nonzero $\boldsymbol{q}$ modes with $r_{g,n} = |\delta F(t_{n+1}^-)|_g$:

$$\delta f_k^\alpha(\boldsymbol{q}, t_{n+1}) = \frac{A_{\rm tar}}{r_{g,n}} \delta f_k^\alpha(\boldsymbol{q}, t_{n+1}^-) \tag{67}$$

for all $\alpha$, $k$, and nonzero $\boldsymbol{q}$. This yields

$$\Lambda_{g,n} = \frac{1}{\mathcal{T}} \ln\left(\frac{r_{g,n}}{A_{\rm tar}}\right), \tag{68}$$

and the global Floquet exponent is given by the late-time average $\Lambda_g = \langle \Lambda_{g,n} \rangle_n$.

In this method, the deviation $\delta F(t)$ aligns with the most unstable mode. Numerically we confirm the relation

$$\Lambda_g = \max_{\boldsymbol{q}} \Lambda(\boldsymbol{q}), \tag{69}$$

which provides a direct consistency check of the two methods.

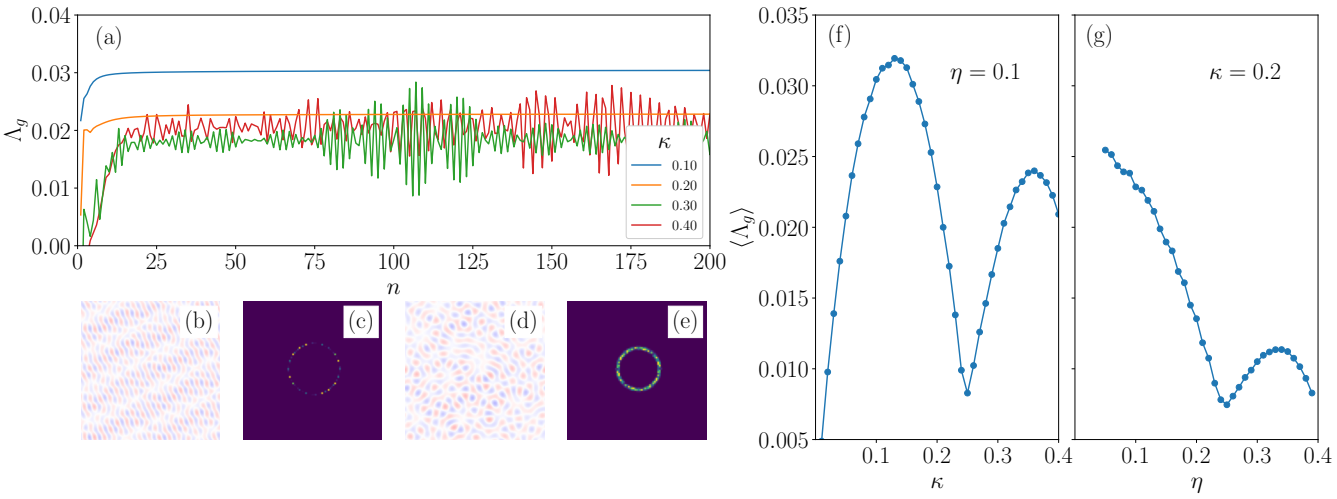


FIG. 12. Global Floquet stability analysis of the homogeneous chiral limit cycle by power iteration for $L = 256$. (a) Time series of the instantaneous global growth rate $\Lambda_{g,n}$ over renormalization steps $n$ for $\eta = 0.1$. (b) and (d) Representative dominant perturbation patterns of $\delta_0^A - \delta_0^B$ in real space after 1000 iterations. (c) and (e) Corresponding Fourier-space patterns, shown in a zoomed-in window defined by $-\pi/3 < q_x < \pi/3$ and $-\pi/3 < q_y < \pi/3$. (f) and (g) Late-time averaged global Floquet exponent $\Lambda_g$ as a function of $\kappa$ and $\eta$, respectively. Parameters: $\kappa = 0.1$ for (b) and (c), $\kappa = 0.4$ for (d) and (e).

As shown in Fig. 12(a), the instantaneous global growth rate converges rapidly and with little residual noise for weak to moderate nonreciprocity, but becomes much more irregular at larger $\kappa$. In particular, the iterations for $\kappa = 0.10$ and 0.20 settle quickly to nearly constant values, whereas $\kappa = 0.30$ and 0.40 display much stronger fluctuations over many renormalization steps.

The corresponding dominant perturbation patterns are shown in Figs. 12(b)–(e). Accordingly, the late-time perturbation field selects a single leading mode, or one representative of a symmetry-related set of equally unstable modes, from the full unstable sector. As $\kappa$ or $\eta$ increase, the selected mode changes in a manner consistent with the branch competition already identified in the local spectrum.

The late-time averaged exponent $\Lambda_g$ exhibits a pronounced dip around $\kappa \simeq 0.25$ at fixed $\eta = 0.1$ [Fig. 12(f)]. At fixed $\kappa = 0.2$, it also shows a clear dip at an intermediate noise level around $\eta = 0.25$ [Fig. 12(g)]. These nonsmooth features indicate a crossover between two distinct instability branches.

### E. Crossover between two unstable modes

To characterize the mode selection associated with this crossover more directly, we track the wavelength

$$\ell_m = \frac{2\pi}{|\boldsymbol{q}_m|}, \tag{70}$$

where $\boldsymbol{q}_m$ is the wavevector of the dominant perturbation peak after convergence of the global power iteration.

Figure 13(a) shows that the selected wavelength quickly saturates with system size for each $\kappa$, indicating that it remains finite in the large-system limit. Figure 13(b) further shows that $\ell_m$ undergoes a clear jump as a function of $\kappa$, and that the location of this jump shifts to larger $\kappa$ as the noise amplitude $\eta$ is increased. This behavior mirrors the dip structure already visible in the leading global Floquet exponent.

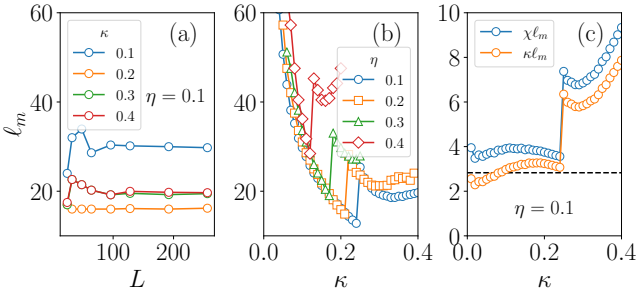


FIG. 13. Selected wavelength $\ell_m$ of the dominant Floquet perturbation. (a) $\ell_m$ as a function of system size $L$ at fixed $\eta = 0.1$. (b) $\ell_m$ as a function of $\kappa$ for several values of $\eta$. (c) Scaled combinations $\chi\ell_m$ and $\kappa\ell_m$ versus $\kappa$ at fixed $\eta = 0.1$. The horizontal dashed line marks the geometric value $2\sqrt{2}$.

In the weak-nonreciprocity branch, the selected wavelength remains controlled by the same geometric scale as the microscopic finite-size crossover. In particular, the combination $\chi\ell_m$ stay close to the geometric value $2\sqrt{2}$. Across the branch-switching point, both scaled quantities jump upward and the simple proportionality breaks down. The global power iteration therefore selects two qualitatively different leading modes on the two sides of the crossover.

This distinction is also visible in the direct time evolution of the Boltzmann equation. The weak-

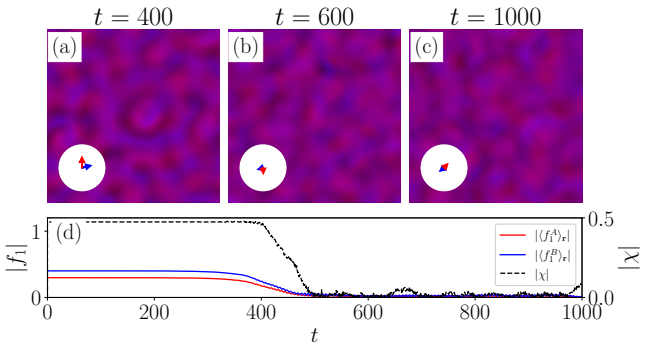


FIG. 14. Representative time evolution from a spatially homogeneous chiral state with a weak added spatial perturbation in the Boltzmann kinetic description at fixed $\eta = 0.1$ and $\kappa = 0.4$. Panels (a)–(c) show spatial snapshots at successive times, while panel (d) shows the time series of the species polarization magnitudes and the global chirality. Compared with the weak-coupling case in Fig. 10, the breakdown is earlier and proceeds through broader, more labyrinthine modulations.

nonreciprocity branch, illustrated by Fig. 10 for $\kappa = 0.2$ at fixed $\eta = 0.1$, develops comparatively sharp finite-wavelength structures and localized spiral-defect-like patterns. The decay of the global chirality is correspondingly delayed and occurs together with the growth and interaction of these localized structures. This weak-nonreciprocity branch is also the one that most closely resembles the breakdown patterns observed in the microscopic simulations.

By contrast, the stronger-nonreciprocity evolution shown in Fig. 14 is dominated by broader long-wavelength modulations and a more abrupt loss of chirality. The resulting structures are more diffuse and labyrinthine, consistent with the broad low-$q$ unstable band identified in the local Floquet spectrum and with the branch switch inferred from the dip of the leading global exponent and the jump in the selected wavelength.

These results support interpreting the transition near intermediate $\kappa$ not as a gradual deformation of a single unstable mode, but as a crossover between two qualitatively different unstable modes and the corresponding nonlinear patterns they generate.

## IX. LARGEST LYAPUNOV EXPONENT ON CHAOTIC STATE

### A. Measurement protocol

To characterize the chaoticity of the system, we measure the largest Lyapunov exponent using the standard rescaling method for nearby trajectories [11, 12]. The numerical procedure is analogous to the global rescaling protocol introduced in Sec. VIII D, but the reference trajectory is now a chaotic trajectory instead of the homogeneous chiral limit cycle.

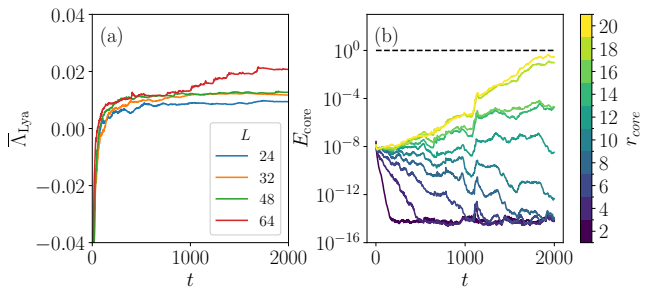


FIG. 15. (a) Cumulative time-averaged largest Lyapunov exponent, $\overline{\Lambda}_{\rm Lya}(t)$, for several system sizes. (b) Core mismatch $E_{\rm core}$ versus time for different $r_{\rm core}$. Parameters: $\eta = 0.1$ and $\kappa = 0.35$.

Starting from an initial state, the system is first evolved until it reaches a stationary state at time $t = t_0$. A configuration at this moment is used as an initial configuration for a base trajectory $F_{\rm base}(t) = \left\{\hat{f}^{\alpha}_{k,\rm base}(\boldsymbol{q},t)\right\}$. A twin trajectory $F_{\rm twin}(t) = \left\{\hat{f}^{\alpha}_{k,\rm twin}(\boldsymbol{q},t)\right\}$ is prepared by adding a random perturbation at $t = t_0$. The deviation of the twin trajectory from the base trajectory is denoted by $\delta F(t) = \{\delta f^{\alpha}_{k}(\boldsymbol{q},t)\}$ with

$$\delta f^{\alpha}_{k}(\boldsymbol{q},t) = \hat{f}^{\alpha}_{k,\rm twin}(\boldsymbol{q},t) - \hat{f}^{\alpha}_{k,\rm base}(\boldsymbol{q},t). \tag{71}$$

The magnitude of an initial perturbation set to a target value $A_{\rm tar}$ as

$$|\delta F(t_0)|_g = A_{\rm tar} \tag{72}$$

using the magnitude defined in Eq. (66).

The base and twin trajectories are then evolved independently while the twin trajectory is reset by rescaling $\delta F(t)$ at times $t_n = t_0 + n\tau_{\rm re}$ with a rescaling time $\tau_{\rm re}$. At $t = t_{n+1}$, all the retained Fourier modes in $\delta F$ are rescaled according to

$$\delta f^{\alpha}_{k}(\boldsymbol{q},t_{n+1}) \to \frac{A_{\rm tar}}{r_{g,n}}\, \delta f^{\alpha}_{k}(\boldsymbol{q},t_{n+1}) \tag{73}$$

with

$$r_{g,n} = |\delta F(t_{n+1})|_g \tag{74}$$

Iterating this procedure, we obtain a sequence of the finite-time growth rate

$$\Lambda_{\rm Lya,n} = \frac{1}{\tau_{\rm re}} \ln\left(\frac{r_{g,n}}{A_{\rm tar}}\right). \tag{75}$$

Throughout this section, we use $t_0 = 1000$ and $\tau_{\rm re} = 1$.

Unlike in the Floquet analysis, no periodic reference orbit is involved here. Accordingly, $\Lambda_{\rm Lya}$ measures the average exponential sensitivity to initial conditions within the chaotic state itself.

### B. Numerical result

The growth rates $\Lambda_{\mathrm{Lya,n}}$ fluctuate strongly. Thus it is useful to consider a cumulative time average

$$\overline{\Lambda}_{\mathrm{Lya}}(t_N) = \frac{1}{N}\sum_{n=1}^{N}\Lambda_{\mathrm{Lya,n}}, \tag{76}$$

which converges at late times to the largest Lyapunov exponent $\Lambda_{\mathrm{Lya}}$.

Figure 4 (a) in the main text and Figure 15 (a) show $\overline{\Lambda}_{\mathrm{Lya}}(t)$ for several system sizes at fixed $\eta = 0.1$. For both $\kappa = 0.2$ (Fig. 4(a)) and $\kappa = 0.35$ (Fig. 15(a)), the cumulative time average approaches a positive value at late times. This provides direct evidence of exponential sensitivity to initial conditions in the statistically stationary state and confirms that the irregular late-time state is chaotic.

## X. MASTER-SLAVE PROTOCOL FOR PROBING THE CHAOTIC LENGTH

The purpose of master-slave construction is to use the breakdown of synchronization as an operational probe of a finite chaotic length in the chaotic kinetic dynamics.

We first generate a chaotic trajectory of the Boltzmann equation, which we refer to as a *master*. From a snapshot of this trajectory at time $t = t_0 = 0$, we prepare a second copy, called a *slave*, by adding a small perturbation to the master. The master then evolves according to the original kinetic equation, while the slave evolves under an additional uni-directional coupling from the master. We introduce a circular region, called a *free core*, of radius $r_{\mathrm{core}}$. Outside the free core, the slave is relaxed toward the master, whereas inside the core it evolves independently. In this way, we can probe a length scale for spatial chaos beyond, which chaotic dynamics is uncorrelated.

Related one-way-coupling constructions have previously been used to study synchronization in spatiotemporally chaotic partial differential equations and in turbulence. For example, unidirectionally coupled chaotic PDEs can synchronize under forcing applied only at a finite number of spatial points, and in fully developed turbulence the small-scale modes were shown to be slaved to the chaotic evolution of larger-scale modes [13, 14].

Our purpose here is different, we ask at what core size synchronization ceases. In this sense, the present construction is closer in spirit to the chaotic-element approach of Ref. [15]. The authors used a unidirectionally coupled reference-target setup to define a characteristic chaotic length in a spatio-temporal chaotic system.

### A. Numerical implementation

In the numerical implementation, the one-way unidirectional coupling is applied in real space to all species and to all retained angular Fourier modes. More specifically, at times $t_n = t_0 + n\Delta t_{\mathrm{nu}}$, the slave field, denoted by $f_{\mathrm{S}}$, is updated according to

$$f^{\alpha}_{\mathrm{S},k}(\boldsymbol{r}) \to f^{\alpha}_{\mathrm{S},k}(\boldsymbol{r}) - \alpha_{\mathrm{nu}} W(\boldsymbol{r})\left[\delta f^{\alpha}_{\mathrm{nu},k}(\boldsymbol{r})\right], \tag{77}$$

where $\alpha_{\mathrm{nu}}$ denotes the nudging strength and $\delta f^{\alpha}_{\mathrm{nu,k}}(\boldsymbol{r}) := f^{\alpha}_{\mathrm{S},k}(\boldsymbol{r}) - f^{\alpha}_{\mathrm{M},k}(\boldsymbol{r})$ is a deviation from a master state, denoted by $f_{\mathrm{M}}$. The free core is incorporated in terms of a spatial mask function $W(\boldsymbol{r})$ given by

$$W(\boldsymbol{r}) = \begin{cases} 0, & |\boldsymbol{r}| \le r_{\mathrm{core}}, \\ 1, & |\boldsymbol{r}| \ge r_{\mathrm{core}} + r_{\mathrm{buf}}, \\ \frac{1}{2}\left[1 - \cos\left(\pi \frac{|\boldsymbol{r}| - r_{\mathrm{core}}}{r_{\mathrm{buf}}}\right)\right], & \text{otherwise.} \end{cases} \tag{78}$$

With this choice, the slave evolves independently inside the free core ($r < r_{\mathrm{core}}$). Outside the core, the coupling is turned on smoothly through a buffer region of width $r_{\mathrm{buf}}$. This buffer region, interpolating the two regions, reduces numerical artifacts.

To quantify whether the slave inside the free core synchronizes with the master, we measure a mismatch

$$E_{\mathrm{core}}(t) = \left[\frac{\sum_{\alpha,k,\boldsymbol{r}} I_{\mathrm{core}}(\boldsymbol{r})\left|\delta f^{\alpha}_{\mathrm{nu,k}}(\boldsymbol{r},t)\right|^2}{\sum_{\alpha,k,\boldsymbol{r}} I_{\mathrm{core}}(\boldsymbol{r})\left|f^{\alpha}_{\mathrm{M},k}(\boldsymbol{r},t)\right|^2}\right]^{1/2}, \tag{79}$$

where

$$I_{\mathrm{core}}(\boldsymbol{r}) = \begin{cases} 1, & |\boldsymbol{r}| \le r_{\mathrm{core}}, \\ 0, & |\boldsymbol{r}| > r_{\mathrm{core}}. \end{cases} \tag{80}$$

is an indicator function for an interior of the free core.

The interpretation of the protocol is then straightforward. If the core is smaller than the intrinsic chaotic length, the exterior determines the dynamics of the interior and the slave synchronizes with the master. Then, $E_{\mathrm{core}}(t)$ decays toward zero. If, on the other hand, the core is larger than the intrinsic chaotic length, the interior sustains its own nonlinear chaotic degrees of freedom and the mismatch grows and maintains $\mathcal{O}(1)$ value. The crossover between these two regimes provides a method estimating the chaotic length.

### B. Numerical results

We use $t_{\mathrm{nu}} = 1$, $\alpha_{\mathrm{nu}} = 0.9$, and $r_{\mathrm{buf}} = 1$ for Fig. 15 (b) and Fig. 4 of the main text. In Fig. 4 with $\kappa = 0.2$, synchronization or desynchronization of the slave core is clearly resolved within the displayed time window. For small core radius $r_{\mathrm{core}}$, the core mismatch $E_{\mathrm{core}}(t)$ decays rapidly toward zero, indicating that the imposed exterior is sufficient to synchronize the freely evolving interior. For larger $r_{\mathrm{core}}$, by contrast, $E_{\mathrm{core}}(t)$ grows to $\mathcal{O}(1)$, showing that the core develops its own chaotic dynamics.

We have also checked that the same qualitative picture persists at larger non-reciprocity, for example at $\kappa = 0.35$. In that case, the time dependence of $E_{\rm core}(t)$ is relatively slower than for $\kappa = 0.2$, so that the approach to synchronization or the growth toward a finite mismatch develops over a longer time window. Nevertheless, the tendency remains clear: for sufficiently small cores $E_{\rm core}(t)$ decreases toward zero, whereas for larger cores it increases.

## XI. NUMERICAL DETAILS FOR THE INTEGRATION OF THE BOLTZMANN EQUATIONS

The Boltzmann hierarchy is integrated numerically using a fourth-order Runge–Kutta scheme with time step $\Delta t = 0.01$. Using smaller time steps produces no qualitative change. For both the long-time kinetic simulations and the Floquet calculations, the angular hierarchy is truncated at $k_m = 4$, whereas $k_m = 50$ is used for the spatially homogeneous solution shown in Fig. 8. The spatial Fourier modes are treated with the standard 2/3 dealiasing rule in order to avoid aliasing errors in the nonlinear terms. For the Floquet and Lyapunov power iterations, we use a target perturbation amplitude $A_{\rm tar} = 10^{-6}$ for both the local and global protocols. We verified that changing $A_{\rm tar}$ from $10^{-6}$ to $10^{-7}$ does not affect the measured exponents within numerical accuracy, confirming that the calculations remain in the linear regime. For the numerical integrations, we use grid spacing $\Delta_x = \Delta_y = 1$ in the Floquet analysis, $\Delta_x = \Delta_y = 1/4$ for the long-time visualizations, and $\Delta_x = \Delta_y = 1/8$ for the Lyapunov exponent estimation and the master-slave method.

For long-time visualizations, Lyapunov exponent estimations, and the master-slave method, we additionally include a small stabilizing diffusion term,

$$\partial_t f_k^\alpha \to \partial_t f_k^\alpha + D_t \nabla^2 f_k^\alpha, \tag{81}$$

with $D_t = 0.1$. Although this term is from discrete time dynamics [16], it is useful for preventing numerical blow-up in extremely dense regions of the chaotic regime. It is not included in the extraction of Floquet exponents.

## XII. SUPPLEMENTAL VIDEOS

Seven supplemental videos accompany this work.

- Video 1 (FIG1_L64.mp4): Microscopic time evolution corresponding to Fig. 1(a)–(c) in the main text. The left panel shows the density field, with RGB channels given by $(\rho_A, 0, \rho_B)$. The middle and right panels show the momentum fields of species $A$ and $B$, respectively.
- Video 2 (FIG1_L256.mp4): Microscopic time evolution corresponding to Fig. 1(d)–(f) in the main text.
- Video 3 (FIG1_L1024.mp4): Microscopic time evolution corresponding to Fig. 1(g)–(i) in the main text.
- Video 4 (SUPFIG10.mp4): Time evolution of the Boltzmann equation corresponding to Fig. 10 of this Supplemental Material.
- Video 5 (SUPFIG14.mp4): Time evolution of the Boltzmann equation corresponding to Fig. 14 of this Supplemental Material.
- Videos 2–5 have the same panel layout as Video 1.
- Video 6 (FIG4_Small_Core.mp4): Time evolution of the Boltzmann equation corresponding to Fig. 4(d) in the main text. The solid line indicates the free core, and the dashed line marks the outer boundary of the buffer region.
- Video 7 (FIG4_Large_Core.mp4): Time evolution of the Boltzmann equation corresponding to Fig. 4(e) in the main text. The solid line indicates the free core, and the dashed line marks the outer boundary of the buffer region.


[1] C. Myin and B. Mahault, Flocking in weakly non-reciprocal mixtures, arXiv preprint arXiv:2510.25377 10.48550/arXiv.2510.25377 (2025).

[2] M. Fruchart, R. Hanai, P. B. Littlewood, and V. Vitelli, Non-reciprocal phase transitions, Nature **592**, 363 (2021).

[3] A. N. Kolmogorov, A refinement of previous hypotheses concerning the local structure of turbulence in a viscous incompressible fluid at high reynolds number, Journal of Fluid Mechanics **13**, 82 (1962).

[4] U. Frisch, *Turbulence: the legacy of A. N. Kolmogorov* (Cambridge University Press, 2010).

[5] H. H. Wensink, J. Dunkel, S. Heidenreich, K. Drescher, R. E. Goldstein, H. Löwen, and J. M. Yeomans, Mesoscale turbulence in living fluids, Proceedings of the National Academy of Sciences **109**, 14308 (2012).

[6] R. Alert, J. Casademunt, and J.-F. Joanny, Active turbulence, Annual Review of Condensed Matter Physics **13**, 143 (2022).

[7] D. Ruelle, Large volume limit of the distribution of characteristic exponents in turbulence, Communications in Mathematical Physics **87**, 287 (1982).

[8] E. Bertin, M. Droz, and G. Grégoire, Boltzmann and hydrodynamic description for self-propelled particles, Physical Review E **74**, 022101 (2006).

[9] E. Bertin, M. Droz, and G. Grégoire, Hydrodynamic

equations for self-propelled particles: microscopic derivation and stability analysis, Journal of Physics A: Mathematical and Theoretical **42**, 445001 (2009).

[10] D. Barkley and R. D. Henderson, Three-dimensional floquet stability analysis of the wake of a circular cylinder, Journal of Fluid Mechanics **322**, 215 (1996).

[11] I. Shimada and T. Nagashima, A numerical approach to ergodic problem of dissipative dynamical systems, Progress of theoretical physics **61**, 1605 (1979).

[12] G. Benettin, L. Galgani, A. Giorgilli, and J.-M. Strelcyn, Lyapunov characteristic exponents for smooth dynamical systems and for hamiltonian systems; a method for computing all of them. part 1: Theory, Meccanica **15**, 9 (1980).

[13] L. Kocarev, Z. Tasev, and U. Parlitz, Synchronizing spatiotemporal chaos of partial differential equations, Physical Review Letters **79**, 51 (1997).

[14] C. C. Lalescu, C. Meneveau, and G. L. Eyink, Synchronization of chaos in fully developed turbulence, Physical Review Letters **110**, 084102 (2013).

[15] A. Karimi and M. R. Paul, Length scale of a chaotic element in rayleigh-bénard convection, Physical Review E—Statistical, Nonlinear, and Soft Matter Physics **86**, 066212 (2012).

[16] B. Mahault, *Outstanding problems in the statistical physics of active matter*, Ph.D. thesis, Université Paris Saclay (COmUE) (2018).